3

Laser Technology for Compact, Narrow-bandwidth Gamma-ray Sources

Miroslav Shverdin, Felicie Albert, David Gibson, Mike Messerly,
Fred Hartemann, Craig Siders, Chris Barty
Lawrence Livermore National Lab
USA

1. Introduction

Compton-scattering is a well-known process, observed and described by Arthur H. Compton in 1924, where the energy of an incident photon is modified by an inelastic scatter with matter (Compton, 1923). In 1948, Feenberg and Primakoff presented a theory of Compton backscattering, where photons can gain energy through collisions with energetic electrons (Feenberg & Primakoff, 1948). In 1963, Milburn and Arutyanyan and Tumanyan developed a concept for Compton-scattering light sources based on colliding an accelerated, relativistic electron beam and a laser (Arutyunyan & Tumanyan, 1964; Milburn, 1963).

When an infrared photon scatters off a relativistic electron beam, its wavelength can be Doppler-upshifted to X-rays. Under properly designed conditions, we can generate high brightness, high flux, MeV-scale photons by colliding an intense laser pulse with a high quality, electron beam accelerated in a Linac. Despite being incoherent, the Compton-generated gamma-rays share many of the laser light characteristics: low divergence, high flux, narrow-bandwidth, and polarizability. Traditional laser sources operate in a $0.1-10$ eV range, overlapping most of the molecular and atomic transitions. Transitions inside the nucleus have energies greater than 0.1 MeV. By matching the gamma-ray energy to a particular nuclear transition, we can target a specific isotope, akin to using a laser to excite a particular atomic or molecular transition.

Narrow-bandwidth gamma-ray sources enable high impact technological and scientific missions such as isotope-specific nuclear resonance fluorescence (NRF) (Bertozzi & Ledoux, 2005; Pruet et al., 2006), radiography of low density materials (Albert et al., 2010), precision nuclear spectroscopy (Pietralla et al., 2002), medical imaging and treatment (Carroll et al., 2003; Bech et al., 2009), and tests of quantum chromodynamics (Titov et al., 2006). In traditional X-ray radiography, the target must have a higher atomic number than the surrounding material. Hence, one could conceal an object by shielding with a higher Z-number material. In NRF gamma-ray imaging, the MeV class photons have very long absorption lengths and will transmit through meter lengths of material unless resonantly absorbed by a specific isotope. Some applications of NRF tuned gamma-rays include nuclear waste imaging and assay, monitoring of special nuclear material for homeland security, and tumor detection for medical treatment.

Compton-based sources are attractive in the 100 keV and higher energy regime because they are highly compact and can be more than 15 orders of magnitude brighter than alternative methods for producing photons in this energy regime: Bremsstrahlung radiation

or synchrotron sources. A major challenge for Compton-scattering based gamma-ray generation is its inefficiency, caused by the low Thomson scattering cross-section. In a typical Compton interaction, only 1 in 10^{10} of the incident laser photons is converted to gamma-rays. Producing a high gamma-ray flux requires a highly energetic, intense, short-pulse laser, precisely synchronized to the electron beam with sub-picosecond precision. Production of high brightness gamma-rays also requires a high quality, low emittance, and low energy spread electron beam. The electron beam is typically generated in a Linac, by accelerating electron bunches produced by the photoelectric effect at a photocathode RF gun. For optimum, high charge electron generation, the few picosecond duration photocathode laser must operate above the photocathode material work function (3.7 eV or 265 nm for copper), and have a flattop spatial and temporal shape.

While various Compton-scattering based sources have been in existence since 1970s, they suffered from low brightness, low flux, and wide bandwidth. Recent advances in laser and accelerator technology have enabled production of high-flux, narrow-bandwidth gamma-ray sources with a highly compact footprint machine. For example, at Lawrence Livermore National Lab, we have recently demonstrated a 2^{nd} generation monoenergetic gamma-ray (MEGa-Ray) source termed T-REX (Thomson-Radiated Extreme X-rays) with a record peak brilliance of 1.5x10^{15} photons/mm^2/mrad^2/s/0.1% bandwidth at 478 keV (Albert et al., 2010). In this chapter, we will give a brief overview of Compton-scattering and describe the laser-technology for MEGa-ray sources with emphasis on a recently commissioned T-REX machine, at LLNL (Gibson et al., 2010). We will review basic concepts, such as Chirped Pulse Amplification (CPA), pulse dispersion and compression, and nonlinear frequency conversion in the context of compact Compton sources. We will also describe some of the novel CPA developments such as hyper-dispersion stretching and compression, and narrowband CPA with Nd:YAG amplifiers that have recently been demonstrated in our group (Shverdin, Albert, Anderson, Betts, Gibson, Messerly, Hartemann, Siders & Barty, 2010). We will conclude with a brief overview of areas for future laser research for the continuing improvement of source size, brightness, flux, efficiency, and cost.

2. Overview of Compton scattering

2.1 Basic properties

Compton scattering sources, which have been widely studied over the past decades (Esarey et al., 1993; Hartemann & Kerman, 1996; Leemans et al., 1997), rely on energy-momentum conservation, before and after scattering. The energy of the scattered photons, E_x, depends on several electron and laser beam parameters:

$$E_x = \frac{\gamma - \sqrt{\gamma^2 - 1}\cos\phi}{\gamma - \sqrt{\gamma^2 - 1}\cos\theta + \bar{\lambda}k_0(1 - \cos\theta\cos\phi + \cos\psi\sin\theta\sin\phi)} E_L \tag{1}$$

where γ is the electron relativistic factor, ϕ is the angle between the incident laser and electron beams, θ is the angle between the scattered photon and incident electron, ψ the angle between the incident and scattered photon, $k_0 = 2\pi/\bar{\lambda}_c$ is the laser wavenumber (reduced Compton wavelength $\bar{\lambda}_c = 3.8616 \times 10^{-13}$ m), and finally E_L is the laser energy. Here, we assume that $\beta = v/c \simeq 1$, where v is the electron velocity. For a head-on collision ($\phi = 180^\circ$) and on-axis observation in the plane defined by the incident electron and laser beams ($\theta = 0^\circ$ and $\psi = 0$), the scattered energy scales as $4\gamma^2 E_L$. In our experiments, where $\gamma \simeq 200$, $k_0 \simeq 10^7$, we can

ignore the electron recoil term, $4\gamma k_0 \bar{\lambda}_c$. One can obtain high-energy (MeV) scattered photons with relatively modest electron beam energies in a compact footprint machine.
When the laser and the electron focal spots, w_0, are matched, the number of the generated γ-rays is approximately $N_x = (\sigma/\pi w_0^2) N_L N_e$, where N_L and N_e are respectively the number of laser photons and electrons at the interaction point, and $\sigma = 6.65 \times 10^{-25}$ cm^2 is the Thomson cross-section. In a linear accelerator, the electron beam focal spot size scales with electron energy as $1/\gamma$ and the γ-ray yield scales as γ^2. Compton scattering sources become more efficient at higher energies and produce a highly collimated beam with good energy-angle correlation.

2.2 Modelling

To properly model the Compton scattering spectrum and the broadening effects, we need to consider electrons with a particular phase space distribution interacting with a Gaussian-paraxial electromagnetic wave. For simplification, we can neglect laser's wavefront curvature for interaction geometries with a slow focus ($f/\# > 10$). For a detailed description of our formalism, see (Hartemann, 2002). We first calculate the Compton scattering frequency using the energy-momentum conservation law:

$$\kappa - \lambda = \bar{\lambda}_c (k_\mu q^\mu), \tag{2}$$

where κ and λ are the incident and scattered light cone variables, $k_\mu = (k, 0, 0, k)$ is the incident laser pulse 4-wavevector, and q_μ is the scattered 4-wavevector. Solving this equation for q, we obtain q_c, the wavenumber for the scattered radiation in spherical coordinates (θ, ϕ):

$$q_c = \frac{k(\gamma - u_z)}{\gamma - u_z \cos\theta + k\bar{\lambda}_c (1 - u_x \sin\theta \cos\phi - u_y \sin\theta \sin\phi - u_z \cos\theta)}, \tag{3}$$

where $u_\mu = (\gamma, u_x, u_y, u_z)$ is the electron 4-velocity. For a counter-propagating geometry, $\theta = \pi$ and $\phi = 0$. Next, we generate a random normal distribution of particles with velocities u_x, u_y, relativistic factor γ and with respective standard deviations $\Delta u_x = j\epsilon_x/\sigma_x$, $\Delta u_y = j\epsilon_y/\sigma_y$ and Δ_γ. The quantities ϵ and σ refer to the electron beam normalized emittance and spot size. j is the jitter: e. g. $j = 1$ in the absence of jitter. Electron beam jitter and emittance are the biggest contributors to the spectral broadening. An example of a normalized spectrum calculated with the method outlined above is shown in Fig. 1. An experimental spectrum from our T-REX source, measured with a germanium detector collecting photons scattered at 48 degrees from an aluminium plate is shown in Fig. 2 (Albert et al., 2010). The γ-ray beam profile is shown in Fig. 2 inset.
From Fig. 2, the spectrum has several distinctive features. The tail after 400 keV is mainly due to the high energy Bremsstrahlung and to pile-up (multiple-photon events) in the detector. The main peak has a maximum at 365 keV, which corresponds to an incident energy of 478 keV. The full width at half maximum of this peak is 55$\pm$5 keV, which corresponds to a relative bandwidth of 15%. The bandwidth of the γ-ray spectrum increases as the square of the normalized emittance - critical for the design of a narrow bandwidth Compton scattering source. The energy spread and jitter of the laser are negligible, while those of the electron beam are 0.2% and $j = 2$, respectively. From Eq. 1, the γ-ray spectrum is broadened by 0.4% by the electron beam energy spread. The electron beam divergence, $\epsilon/\gamma r$, where r is the electron beam radius, broadens the γ-ray spectrum by 4.5% At energies below 250 keV, we record a broad continuum with two additonal peaks at 80 keV and 110 keV. These features are artifacts of several processes during beam detection and can be reproduced by a

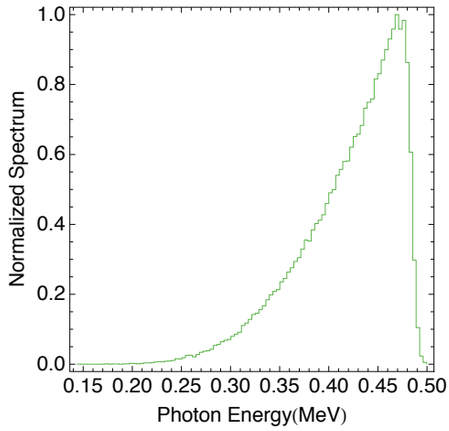

Fig. 1. Example of a spectrum simulated with Mathematica, using 10^5 particles and 100 bins for an electron beam energy of 116 MeV and a laser wavelength of 532 nm. The other parameters are $j = 2$, $\epsilon_x = 5$ mm mrad, $\epsilon_y = 6$ mm mrad, $\sigma_x = 35$ μm and $\sigma_y = 40$ μm.

Monte-Carlo simulation. We utilized MCNP5 code (Forster et al., 2004), with modifications to include Compton scattering of linearly polarized photons (G.Matt et al., 1996) to describe the realistic experimental set-up. Fig. 2 shows the simulated pulse height spectrum expected for single-photon counting. The continuum below 250 keV is caused by incomplete energy absorption (elastic Compton scattering) in the detector itself. The broad peak at 110 keV arises from double Compton scattering off the Al plate and the adjacent wall, followed by photoabsorption in the Ge Detector. Since the detector is shielded with lead, the first peak is due to X-rays coming from the lead K_α and K_β lines, respectively, at 72.8 keV, 75 keV, 84.9 keV and 87.3 keV.

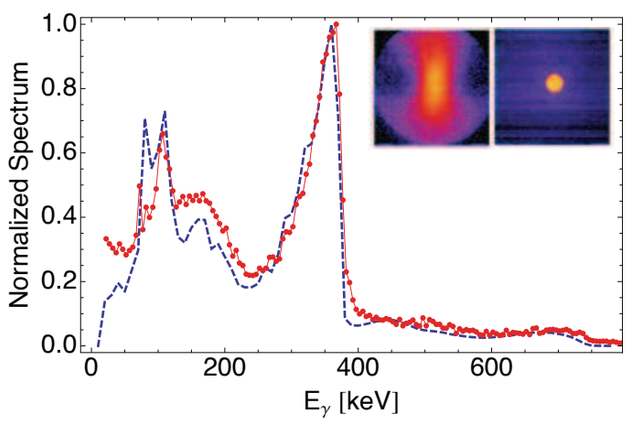

Fig. 2. On axis spectrum recorded after scattering off the Al plate and corresponding Monte Carlo simulation. The images correspond to the full beam and the signal transmitted through the collimator, respectively.

3. Laser technology

3.1 Laser system overview

We describe laser technology underlying high brightness, Compton-scattering based monoenergetic gamma-ray sources, focusing on a recently commissioned T-REX (Gibson et al., 2010) and a 3^{rd} generation Velociraptor, currently under construction at Lawrence

Livermore National Lab. The two main systems of these machines consist of a low emittance, low energy spread, high charge electron beam and a high intensity, narrow bandwidth, counter-propagating laser focused into the interaction region to scatter off the accelerated electrons. A simplified schematic of the Compton-scattering source is shown in Fig. 3.
A state of the art ultrashort laser facilitates generation of a high charge, low emittance electron beam. A photogun laser delivers spatially and temporally shaped UV pulses to RF photocathode to generate electrons with a desired phase-space distribution by the photoelectric effect. Precisely synchronized to the RF phase of the linac, the generated electrons are then accelerated to relativistic velocities. The arrival of the electrons at the interaction point is timed to the arrival of the interaction laser photons. A common oscillator, operating at 40 MHz repetition rate, serves as a reference clock for the GHz-scale RF system of the Linac, seeds both laser systems, and facilitates subpicosecond synchronization between the interaction laser, the photogun laser, and the RF Linac phase. Typical parameters for the laser system are listed in Table 1.

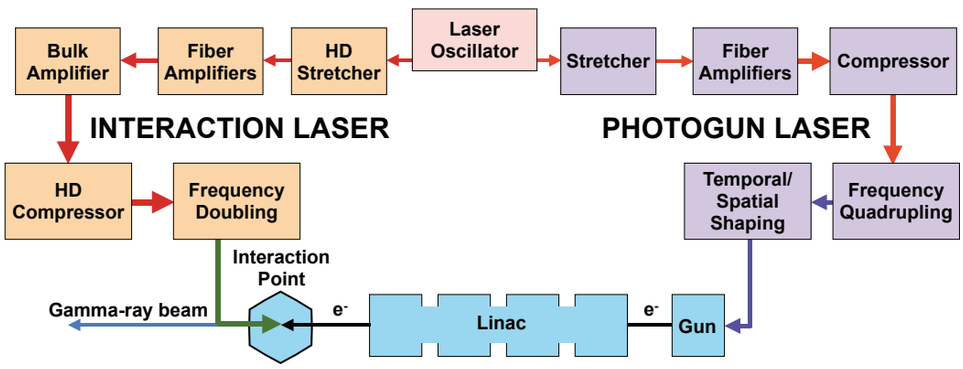

Fig. 3. Block diagram of the Velociraptor compton source with details of the laser systems.

Parameters	Oscillator	Photogun Laser	Interaction Laser
Repetition Rate	40.8 MHz	10-120 Hz	10-120 Hz
Wavelength	1 μm	263 nm	532 nm or 1 μm
Energy	100 pJ	30-50 μJ	150 mJ - 800 mJ
Pulse Duration	1 ps	2 or 15 ps	10 ps
Spot size on target	n/a	1-2 mm dia	20-40 μm RMS

Table 1. Summary of key laser parameters for T-REX and Velociraptor compton source

Because the oscillator produces ultrashort pulses with energies in the pico-Joule to nano-Joule range, and the final required energies are in the milli-joule to Joule range, pulses are amplified by 70-100 dB in a series of amplifiers. Chirped pulse amplification (CPA) enables generation of highly energetic picosecond and femtosecond pulses (Strickland & Mourou, 1985). The key concept behind CPA is to increase the pulse duration prior to amplification, thereby reducing the peak intensity during the amplification process. The peak intensity of the pulse determines the onset of various nonlinear processes, such as self-focusing, self-phase modulation, multi-photon ionization that lead to pulse brake-up and damage to the medium. Nonlinear phase accumulation, or B-integral, is guided by Eq. 4:

$$\phi_{NL} = \frac{2\pi}{\lambda} \int_{-\infty}^{\infty} n_2 I(z) dz \tag{4}$$

where, $I(z)$ is a position dependent pulse intensity and n_2 is the material dependent nonlinear refractive index ($n = n_0 + n_2 I$). ϕ_{NL} should normally be kept below 2-3 to avoid significant pulse and beam distortion. For a desired final pulse intensity, we minimize the value of the accumulated B-integral by increasing the beam diameter and the chirped pulse duration. After amplification, the stretched pulse is recompressed to its near transform limited duration. The four stages of the CPA process are illustrated in Fig. 4. The stretcher and the compressor impart the largest pulse dispersion. In our laser systems, the chirped pulse duration is between 1.5 and 3 ns to maximize the final pulse energy.

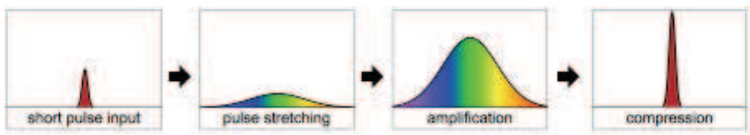

Fig. 4. Basic CPA scheme: ultrashort seed pulse is stretched, amplified, and recompressed.

The photogun laser consists of a mode-locked and phase-locked Yb:doped fiber oscillator, an all-reflective pulse stretcher, and a series of fiber amplifiers producing over 1 mJ/pulse at 10 kHz at the output. The pulses are then re-compressed to near transform limited (200 fs) duration in a compact multi-layer-dielectric grating compressor. Next, two nonlinear crystals generate the 4^{th} harmonic of the fundamental frequency in the UV. Temporally and spatially shaped pulses are finally delivered at the RF photogun.

The interaction laser system (ILS) parameters are optimized to generate high flux, narrowband γ rays. The interaction laser produces joule-class, $\approx$ 10 ps pulses at 1064 nm, at up to 120 Hz repetition rate, which are then frequency doubled to 532 nm. Separate fiber amplifiers pre-amplify the pulses prior to injection into a bulk power amplifier chain. The pulses are then recompressed, frequency doubled, and focused into the interaction region to scatter off the electrons.

Picosecond pulse duration is desirable to both minimize peak laser intensity, which leads to nonlinear scattering effects, and decrease the laser linewidth, $\Delta\omega_{laser}$, which broadens the generated γ-ray bandwidth, $\Delta\omega_\gamma$, as $\Delta\omega_\gamma = \sqrt{\Delta\omega_{res}^2 + \Delta\omega_{laser}^2}$. Here, $\Delta\omega_{res}$ is the contribution to γ-ray bandwidth from all other effects, such as e^- beam emittance, energy spread, focusing geometry, etc. Due to narrow laser pulse bandwidths, we utilize a novel type of high dispersion pulse stretcher and pulse compressor. The ILS pulses are finally frequency doubled to increase the generated γ-ray energy.

Several alternate types of Compton-scattering γ-ray sources, not covered here, exist (see (D'Angelo et al., 2000)). Some utilize different laser technologies such as Q-switched, nanosecond duration interaction laser pulses (Kawase et al., 2008). Other sources are based on Free Electron Laser (Litvinenko et al., 1997) or CO_2 technologies (Yakimenko & Pogorelsky, 2006). Several sources based on low charge, high repetition rate electron bunches and low energy, high repetition rate laser pulses coupled to high finesse resonant cavities have been proposed (Graves et al., 2009) and demonstrated (Bech et al., 2009).

3.1.1 Dispersion management

The action of various dispersive elements is best described in the spectral domain. Given a time dependent electric field, $E(t) = A(t)e^{i\omega_0 t}$, where we factor out the carrier-frequency term, its frequency domain is the Fourier transform, $\mathcal{A}(\omega) = \int_{-\infty}^{\infty} A(t)e^{-i\omega t}dt = \sqrt{I_s(\omega)}e^{i\phi(\omega)}$. Here, we explicitly separate the real spectral amplitude, $\sqrt{I_s(\omega)}$, and phase, $\phi(\omega)$. We

define spectral intensity $I_s(\omega) \equiv |\mathcal{A}(\omega)|^2$, and temporal intensity $I(t) \equiv |A(t)|^2$ We can Taylor expand the phase of the pulse envelope $\mathcal{A}(\omega)$ as

$$\phi(\omega) = \sum_{n=0}^{\infty} \frac{1}{n!} \phi^{(n)}(0) \omega^n \tag{5}$$

where $\phi^{(n)}(0) \equiv \frac{d^n \phi(\omega)}{d\phi^n}$ evaluated at $\omega = 0$. Term n=1 is the group delay, corresponding to the time shift of the pulse; terms $n \geq 2$ are responsible for pulse dispersion. Terms $\phi^{(n)}(0)$, where n=2 and 3, are defined as, respectively, group delay dispersion (GDD) and third order dispersion (TOD). For a gaussian, unchirped, pulse, $E(t) = E_0 e^{-\frac{t^2}{\tau_0^2}}$, we can analytically calculate its chirped duration, τ_f assuming a purely quadratic dispersion ($\phi^{(n)}(0) = 0$ for $n > 2$).

$$\tau_f = \tau_0 \sqrt{1 + 16 \frac{GDD^2}{\tau_0^4}} \tag{6}$$

The transform limited pulse duration is inversely proportional to the pulse bandwidth. For a transform limited gaussian, the time-bandwidth product (FWHM intensity duration [sec] x FWHM spectral intensity bandwidth [Hz]) is $\frac{2}{\pi} \log 2 \approx 0.44$. From Eq. (6), for large stretch ratios, the amount of chirp, GDD, needed to stretch from the transform limit, τ_0, to the final duration, τ_f, is proportional to τ_0.

In our CPA system, near transform limited pulse are chirped from 200 fs (photogun laser) and 10 ps (interaction laser) to few nanosecond durations. Options for such large dispersion stretchers include chirped fiber bragg gratings (CFBG), chirped volume Bragg gratings (CVBG), and bulk grating based stretchers. Prism based stretchers do not provide sufficient dispersion for our bandwidths. The main attraction of CFBG and CVBG is their extremely compact size and alignment insensitivity. Both CFBG and CVBG have shown great recent promise but still have unresolved issues relating to group delay ripple that affect recompressed pulse fidelity (Sumetsky et al., 2002). High pulse contrast systems typically utilize reflective grating stretchers and compressors which provide a smooth dispersion profile. The grating stretcher and compressor designs are driven by the grating equation which relates the angle of incidence ψ and the angle of diffraction ϕ measured with respect to grating normal for a ray at wavelength λ,

$$\sin(\psi) + \sin(\phi) = \frac{m\lambda}{d} \tag{7}$$

where d is the groove spacing and m is an integer specifying the diffraction order. Grating stretchers and compressors achieve large optical path differences versus wavelength due to their high angular resolution, $\frac{d\phi}{d\lambda}$ (Treacy, 1969; Martinez, 1987).

A stretcher imparts a positive pulse chirp (longer wavelengths lead the shorter wavelengths in time) and a compressor imparts a negative pulse chirp. The sign of the chirp is important, because other materials in the system, such as transport fibers, lenses, and amplifiers, have positive dispersion. A pulse with a negative initial chirp could become partially recompressed during amplification and damage the gain medium.

We need to dispersion balance the CPA chain, to recompress the pulse to its transform limit. The total group delay, GD_{total} vs wavelength for the system must be constant at the output, or $GD_{total}(\lambda) = GD_{stretcher}(\lambda) + GD_{compressor}(\lambda) + GD_{fiber}(\lambda) + GD_{oscillator}(\lambda) + GD_{amplifier}(\lambda) + GD_{material}(\lambda) = C_1$, where C_1 is an arbitrary constant. From Eq. (5), $\phi(\omega) = \int_{-\infty}^{\infty} GD(\omega)d\omega$. Any frequency dependence in the total group delay will degrade pulse fidelity.

Several approaches to achieving dispersion balance exist. In the Taylor's expansion (Eq. (5)) of the phase of a well behaved dispersive element, when $n < m$ the contribution of a term n to the total phase is much larger than of a term m, or $|\phi^{(n)}(0)\Delta\omega^n/n!| \gg |\phi^{(m)}(0)\Delta\omega^m/m!|$, where $\Delta\omega$ is the pulse bandwidth. One approach to achieve dispersion balance is to calculate the total GDD, TOD, and higher order terms for the system and attempt to zero them. For example, when terms up to the 4^{th} order are zero, the system is quintic limited. This term-by-term cancellation approach can become problematic when successive terms in the Taylor's expansion do not decrease rapidly. It is often preferable to minimize the residual group delay, GD_{RMS}, over the pulse bandwidth (Eq. 8).

$$GD_{RMS} = \sqrt{\frac{\int_{-\infty}^{\infty} \left(GD(\omega) - \bar{GD}\right)^2 |\mathcal{E}(\omega)|^2 d\omega}{\int_{\infty}^{\infty} |\mathcal{E}(\omega)|^2 d\omega}} \tag{8}$$

where $\bar{GD}$ is the mean group delay, $\bar{GD} \equiv \frac{\int_{-\infty}^{\infty} GD(\omega)|\mathcal{E}(\omega)|^2 d\omega}{\int_{-\infty}^{\infty} |\mathcal{E}(\omega)|^2 d\omega}$.

A sample pulse stretcher is shown in Fig. 5. The stretcher consists of a single grating, a lens of focal length f, a retro-reflecting folding mirror placed f away from the lens and a vertical roof mirror. The folding mirror simplifies stretcher configuration and alignment by eliminating a second grating and lens pair. A vertical roof mirror double passes the beam through the stretcher and takes out the spatial chirp. The total dispersion of the stretcher is determined by the distance from the grating to the lens, L_f. When $L_f = f$, the path lengths at all wavelengths are equal and the net dispersion is zero. When $L_f > f$, the chirp becomes negative, same as in the compressor. In a stretcher, $L_f < f$ producing a positive chirp. We can calculate the dispersion, or $GD(\omega) = n_\omega L(\omega)/c$, where $L(\omega)$ is the frequency dependent propagation distance and n_ω is the frequency dependent refractive index, using various techniques. Here, we give a compact equation for $GDD(\omega) = \partial GD(\omega)/\partial\omega$, from which all other dispersion terms can be determined. Assuming an aberration free stretcher in the thin lens approximate, $GDD(\omega)$ is then given by Eq. 9.

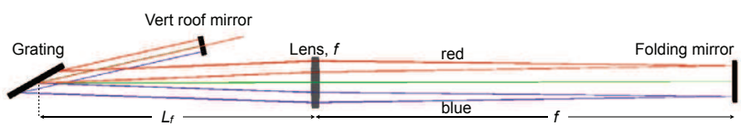

Fig. 5. Grating and lens based stretcher is folded with a flat mirror. The distance from the grating to the focal length of the lens determine the sign and magnitude of the chirp.

$$GDD(\omega) = 2(f - L_f)\frac{\lambda}{\pi c^2}\frac{[\sin(\phi) + \sin(\psi)]^2}{\cos^2(\phi)} \tag{9}$$

where the diffraction angle, ϕ is a function of ω. The aberration free approximation is important, because a real lens introduces both chromatic and geometric beam aberrations which modify higher order dispersion terms from those derived from Eq. 9.

A compressor, which is typically a final component in the CPA system undoes all of the accumulated dispersion. The compressor used on the photogun laser is shown in Fig. 6. Compared to the stretcher, the lens is absent. The magnitude of the negative chirp is now controlled by the distance from the horizontal roof to the grating. The horizontal roof, here folds the compressor geometry and eliminates a second grating. As in the stretcher of Fig. 5, the compressor's vertical roof mirror double passes the beam and removes the spatial chirp. Because a compressor has no curved optics, it introduces no geometric or chromatic aberrations. The dispersion of a real compressor is very precisely described by the Treacy formula or its equivalent given by Eq. 10.

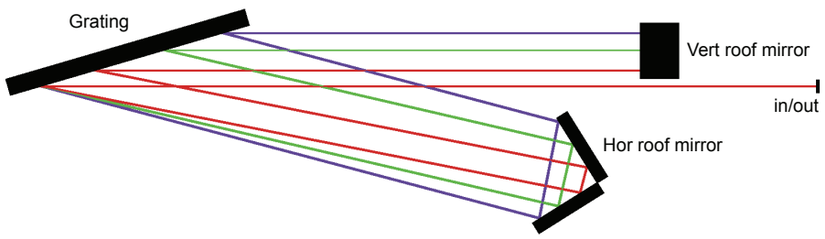

Fig. 6. Folded grating compressor. The distance from the horizontal roof mirror to the grating determines the magnitude of the negative chirp.

$$GDD(\omega) = -L_1 \frac{\lambda}{\pi c^2} \frac{[\sin(\phi) + \sin(\psi)]^2}{\cos^2(\phi)} \tag{10}$$

The actual stretcher design for Velociraptor photogun laser is shown in Fig. 7. The all-reflective Offner design (Cheriaux et al., 1996) uses a convex and a concave mirror to form an imaging telescope with magnification of -1 and relay planes at the radius of curvature (ROC) center of the concave mirror. The grating is placed inside the ROC to impart a positive chirp. A vertical roof mirror folds the stretcher geometry and eliminates the second grating. The Offner stretcher is compact and has low chromatic and geometric aberrations. Consequently, its dispersion profile is nearly aberration free, meaning the GDD and higher order dispersion terms are closely predicted by Eq. 9.

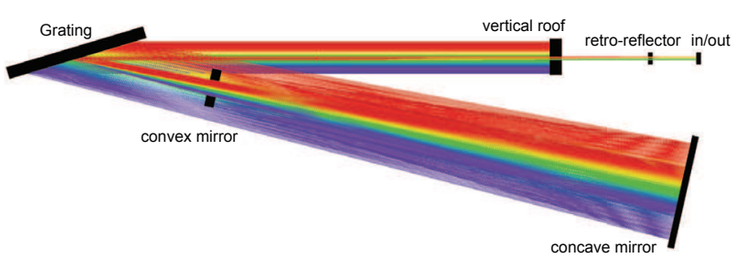

Fig. 7. Raytraced design of the Offner stretcher for the photogun laser on Velociraptor.

3.2 Fiber oscillator and amplifiers

Essential to building a compact, highly stable laser system is a fiber front-end. Fibers lasers are highly portable, reliable, relatively insensitive to external perturbations, provide long term hands free operation, and have been scaled to average powers above 1 kW in a diffraction limited beam (Jeong et al., 2004). When the required pulse energy is above a mJ, a fiber oscillator and amplifiers can serve as a front end in a multi-amplifier-stage system. We employ

a 10 mW Yb:doped mode-locked oscillator which, when compressed, produces 250 pJ, sub 100 fs, near transform limited pulses at 40.8 MHz repetition rate with a full bandwidth from 1035 nm to 1085 nm. The oscillator, based on a design developed at Cornell (Ilday et al., 2003), fits on a rack mounted, 12″x12″ breadboard (see Fig. 8).
On T-REX and Velociraptor, a single fiber oscillator seeds both, the photogun laser and the interaction laser systems. An experimental oscillator spectrum showing the bandpass for the photogun and the interaction lasers is shown in Fig. 9. Two different chains of fiber Yb:doped fiber amplifiers tuned for peak gain at 1053 nm for PDL and 1064 nm for ILS, boost the seed pulse to $\approx$100 μJ/pulse. The seed is chirped to a few nanosecond duration prior to amplification. Each fiber amplifier stage provides 20 dB of gain. The repetition rate is gradually stepped down to 10 kHz with acousto-optic modulators (AOM), inserted in between fiber amplifiers. The AOMs also remove out of band amplified spontaneous emission (ASE), preserving pulse fidelity.
The total energy from the fiber amplifier is limited by the total stored energy and by the accumulated nonlinear phase (Eq. 4). Several initial amplifier stages consist of telecom-type, 6.6 μm core polarization maintaining (PM) fibers. The output from this core sized fiber is limited to $\approx$1μJ. Next, a series of large mode field diameter, 29 μm core photonic band-gap (PBG) fibers accommodate pulse energies up to 100 μJ. We are currently developing even larger core (80 μm) PBG fiber rod based amplifiers to attain over 1 mJ per pulse at the output. A major challenge with PBG and other large core fibers is careful control of the refractive index uniformity to prevent generation of higher order spatial modes, which degrade beam quality.

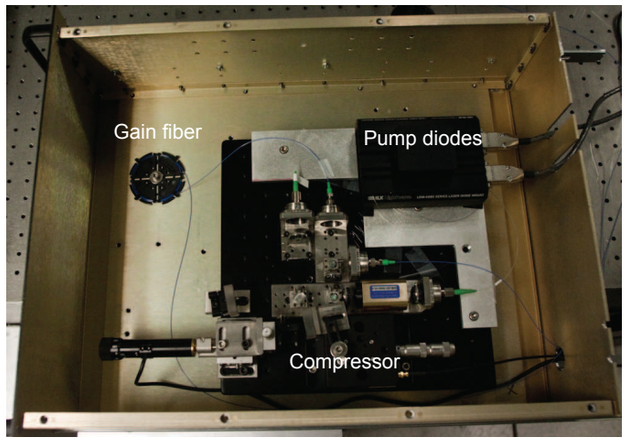

Fig. 8. The ultrashort Yb^+ doped fiber oscillator fits on a 12″x12″ breadboard. When recompressed, the anomalous dispersion oscillator generates 100 fs pulses.

4. Amplification

The action of the amplifier is illustrated in Fig. 10. An input pulse with intensity I_{in} is amplified to output intensity I_{out}. An amplifier can be chacterized by its small signal (undepleted) gain, G_0, saturation fluence, J_{sat}, and its frequency dependent lineshape function, $g(\nu)$. In general, we need to solve the laser rate equations to determine the output pulse shape, spectral distribution, and energy. For a homogeneous gain medium, when (1) the temporal pulse variation and the population inversion is sufficiently small (compared to T_2 coherence time) to justify rate equation analysis, and (2) transient effects relating to spontaneous emission and pumping occur on a time scale much longer than the pulse

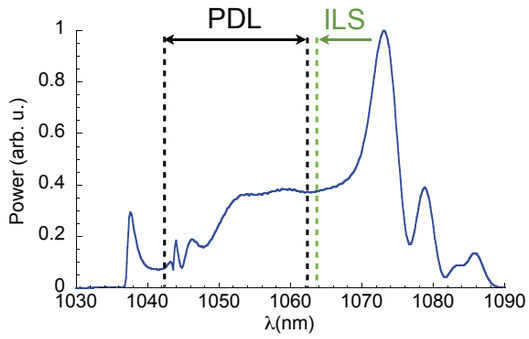

Fig. 9. Experimental pulse spectrum of the Velociraptor oscillator of Fig. 8. The same oscillator seeds both the interaction and the photogun lasers.

duration, an analytical solution can be obtained using a Frantz-Nodvik approach (Frantz & Nodvik, 1963). Eq. (11) is derived for a monochromatic input pulse (Planchon et al., 2005).

$$I_{out}(t) = I_{in}(t) \times \left[1 - \left(1 - G_0^{-1}\right) e^{-J_{in}(t)/J_{sat}(t)}\right]^{-1} \tag{11}$$

Here, $J_{in}(t) \equiv \int_0^t I_{in}(t')dt'$ is the instantaneous fluence. Eq. (11) can be modified to describe amplification of a chirped pulse. This involves determining the frequency dependence of the small gain, $G_0(\nu)$ and the saturation fluence, $J_{sat}(\nu)$, both of which depend on the emission cross-section $\sigma_e(\nu)$. For a four-level system, $J_{sat}(\nu) = h\nu/\sigma_e(\nu)$, and $G_0 = \exp[N\sigma_e(\nu)]$, where N is the population inversion. If the instantaneous pulse frequency, $\bar{\nu} = \frac{1}{2\pi}\frac{d\phi(t)}{dt}$ is a monotonic function of t, we can define time as a function of frequency, $t(\nu)$. In this instantaneous frequency approach, we can rewrite Eq. (11) as a function of ν. Various aspects of chirped pulse amplification, such as total output energy, gain narrowing, square pulse distortion, and spectral sculpting can be analytically calculated using the modified form of Eq. (11).

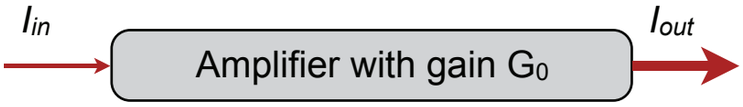

Fig. 10. Basic scheme for pulse amplification. A gain medium with stored energy coherently amplifies the input pulse.

4.1 Chirped pulse amplification with narrowband pulses

In CPA, the gain bandwidth of the amplifying medium is typically broad enough to minimize gain narrowing of the seed pulse. On the photogun laser, Yb doped glass has a wide bandwidth spanning from 1000 nm to 1150 nm, and is well suited for amplifying 100 fs pulses. On the interaction laser, however, bulk amplification is in Nd:YAG, which has a narrow bandwidth of 120 GHz. The seed pulses gain narrow to sub nanometer bandwidths after amplification. Traditional two-grating stretchers and compressors cannot provide adequate dispersion in a table-top footprint. In this section, we will describe novel hyper-dispersion technology that we developed for CPA with sub-nanometer bandwidth pulses (Shverdin, Albert, Anderson, Betts, Gibson, Messerly, Hartemann, Siders & Barty, 2010). The meter-scale stretcher and compressor pair achieve 10x greater dispersion compared to standard two-grating designs. Previously, D. Fittinghoff, *et. al.* suggested hyper-dispersion

compressor arrangements (Fittinghoff et al., 2004). F. J. Duarte described a conceptually similar hyper-dispersion arrangements for a prism-based compressor (Duarte, 1987).
We utilize commercial Nd:YAG amplifiers for two reasons: (1) Nd:YAG technology is extremely mature, relatively inexpensive, and provides high signal gain; (2) nominally 10 ps transform limited laser pulses are well-suited for narrowband γ-ray generation. Employing a hyper-dispersion stretcher and compressor pair, we generated 750 mJ pulses at 1064 nm with 0.2 nm bandwidth, compressed to near transform limited duration of 8 ps.
The nearly unfolded version of the hyper-dispersion compressor is shown in Fig. 11, with a retro-mirror replacing gratings 5-8. Compared to standard Treacy design, this compressor contains two additional gratings (G2 and G3). The orientation of G2 is anti-parallel to G1: the rays dispersed at G1, are further dispersed at G2. This anti-parallel arrangement enables angular dispersion, $\frac{d\theta}{d\lambda}$, which is greater than possible with a single grating. The orientation of G3 and G4 is parallel to, respectively, G2 and G1. G3 undoes the angular dispersion of G2 and G4 undoes the angular dispersion of G1 producing a collimated, spatially chirped beam at the retro-mirror. After retro-reflection, the spatial chirp is removed after four more grating reflections. The number of grating reflections (8), is twice that in a Treacy compressor. High diffraction efficiency gratings are essential for high throughput efficiency. We utilize multi-layer-dielectric (MLD) gratings developed at LLNL with achievable diffraction efficiency >99% (Perry et al., 1995). The magnitude of the negative chirp is controlled by varying L_1, the optical path length of the central ray between G1 and G2 and L_2, the optical path length between G2 and G3.
We derive an analytical formula (Eq. 12) for group delay dispersion (GDD) as a function of wavelength for the compressor using Kostenbauder formalism (Kostenbauder, 1990; Lin et al., 1993).

$$GDD = -\frac{\lambda}{\pi c^2}\frac{\left[\sin(\phi)+\sin(\psi)\right]^2}{\cos^4(\phi)} \times \left[2L_1\cos^2(\phi) + L_2\left[\cos(\phi)+\cos(\psi)\right]^2\right] \tag{12}$$

Here ψ is the angle of incidence and ϕ is the angle of diffraction of the central ray of wavelength λ at the first grating measured with respect to grating normal. We assume that the groove density of gratings 1 and 2 is the same. Note that the expression for GDD reduces to that of the standard two-grating compressor when L_2=0. Higher order dispersion terms can be derived by noting that ϕ is a function of wavelength.

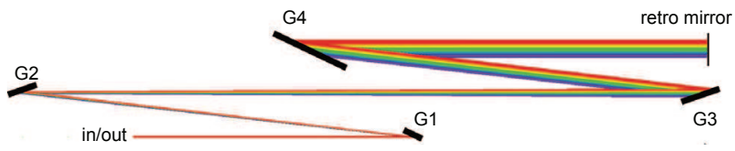

Fig. 11. Unfolded version of the hyper-dispersion compressor with anti-parallel gratings.

Compressor design can be folded to reduce the total number of gratings and simplify compressor alignment. The compressor shown in Fig. 12 has been designed for Velociraptor and is similar to the experimental design on T-REX. The compressor consists of two 40x20 cm multi-layer dielectric (MLD) gratings arranged anti-parallel to each other, a vertical roof mirror (RM), and a series of two periscopes and a horizontal roof mirror. These six mirrors set the height and the position of the reflected beam on the gratings and inverts the beam in the plane of diffraction. The beam is incident at Littrow-3 degrees (64.8^o) on the 1740 grooves/mm

gratings. The vertical roof mirror here, is equivalent to the retro-mirror in Fig. 11. The beam undergoes a total of 8 grating reflections and 16 mirror reflections in the compressor. The total beam path of the central ray is 22 m. On T-REX, the MLD gratings had a diffraction efficiency above 97%, enabling an overall compressor throughput efficiency of 60%. Here, the magnitude of the chirp is tuned by translating the horizontal roof mirror. The compressor, with its relatively compact footprint of 3x0.7 m provides GDD=-4300 ps^2/rad, or a pulse dispersion of 7000 ps/nm. This chirps the incident 0.2 nm bandwidth pulse to 3 ns. The two grating separation in a standard Treacy compressor with the same dispersion would be 32 m.

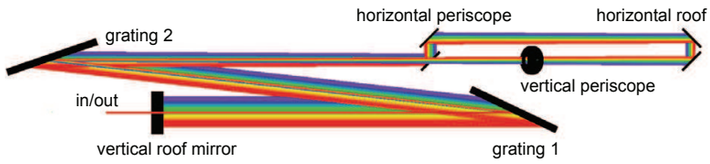

Fig. 12. The compact hyper-dispersion compressor consisting of two 1740 grooves/mm gratings has a footprint of 3 x 0.7 m and group delay dispersion of -4300 ps^2/rad.

The hyper-dispersion stretcher design is conceptually similar. The unfolded version is shown in Fig. 13. Compared to the standard Martinez stretcher, the hyper-dispersion design contain two extra mirrors G1 and G4, arranged anti-parallel to G2 and G3. We define L_f as the path length from G2 to the first lens. Then the total ray path length from G1 to the first lens ($L_1 + L_f$) must be smaller than the lens focal length, f to produce a positive chirp. The magnitude of the chirp is controlled by varying the value of $L_1 + L_f - f$.
We modify Eq. 12 to derive the GDD formula for the aberration free hyper-dispersion stretcher shown in Fig. 13:

$$GDD = -\frac{\lambda}{\pi c^2}\frac{\left[\sin(\phi)+\sin(\psi)\right]^2}{\cos^4(\phi)} \times \left[L_1\cos^2(\phi) + (L_f - f)\left[\cos(\phi)+\cos(\psi)\right]^2\right] \tag{13}$$

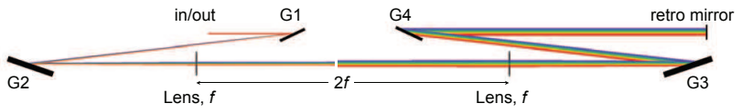

Fig. 13. Unfolded hyper-dispersion stretcher utilizes four gratings, as opposed to two gratings in the standard Martinez design.

The folded CAD version of the stretcher built for T-REX is shown in Fig. 14. For high fidelity pulse recompression, the stretcher is designed with a nearly equal and opposite chirp compared to that of the compressor. The small difference accounts for other dispersive elements in the system. We again use two large 1740 grooves/mm MLD gratings, with footprints of 20x10 cm and 35x15 cm. The beam is incident at the same Littrow-3^o angle as in the compressor. A large, 175 mm diameter, f = 3099 mm lens accommodates the large footprint of the spatially chirped beam. A folding retro-mirror is placed f away from the lens, forming a 2-f telescope seen in the unfolded version of Fig. 13. The beam height changes through off-center incidence on the lens. After 4 grating reflections, the beam is incident on the vertical roof mirror, which is equivalent to the retro-mirror in Fig. 13. The two 45^0

mirrors fold the beam path, rendering a more compact footprint. After 8 grating reflections, the compressed pulse arrives and 2^{nd} pass retro mirror. The beam is then retro-reflected through the stretcher, undergoing a total of 16 grating reflections. We double pass through the stretcher to double the total pulse chirp. Beam clipping on the lens prevents reducing the lens to G2 distance to match compressor dispersion in a single pass.
Chromatic and geometric lens aberrations modify higher order dispersion terms in the stretcher, requiring raytracing for more accurate computation. We use a commercial ray-tracing software (FRED by Photon Engineering, LLC) to compute ray paths in the stretcher and in the compressor. From raytrace analysis, the GDD for the stretcher is 4300 ps^2/rad, and the TOD/GDD ratio is -115 fs, at the 1064 nm central wavelength; for the compressor, the TOD/GDD ratio is -84 fs. The TOD mismatch would result in a 3% reduction in the temporal Strehl ratio of the compressed pulse. We can match the GDD and the TOD of the stretcher/compressor pair by a 1^o increase of the angle of incidence on gratings 1 and 2 in the stretcher.

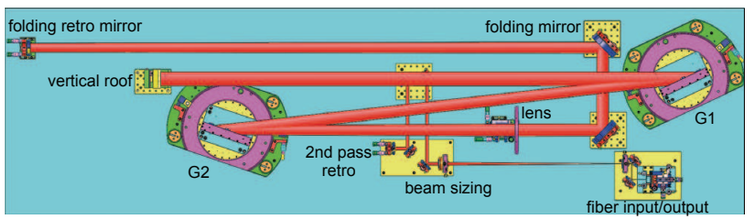

Fig. 14. The compact hyper-dispersion stretcher matches the GDD of the compressor.

We employed the hyper-dispersion stretcher-compressor pair in our interaction laser. Commercial Q-switched bulk Nd:YAG laser heads amplified stretched pulses from the fiber chain to 1.3 J, with 800 mJ remaining after pulse recompression. We characterize the compressed pulse temporal profile using multi-shot second harmonic generation (SHG) frequency resolved optical gating (FROG) (Kane & Trebino, 1993; Kane et al., 1994) technique. FROG is a commonly used method for measurement of ultrashort pulses. Compared to autocorrelation which cannot measure the actual pulse intensity, FROG measures both the intensity and the phase of the recompressed pulse. In its multi-shot, SHG implementation, a FROG measurement consists of measuring the frequency spectrum of the auto-correlation signal at each relative delay between the two pulse replicas. Mathematically, we determine $I^{SHG}_{FROG}(\omega,\tau) = |\int_{-\infty}^{\infty} E(t)E(t-\tau)\exp(-i\omega t)dt|^2$, which is a 2D spectrogram plotting delay, τ vs frequency (Trebino, 2000). Several inversion algorithms exist to process the FROG data and extract pulse intensity and phase.
In the measurement, we use a 0.01 nm resolution 1 m spectrometer (McPherson Model 2061) to resolve the narrow bandwidth pulse spectrum at the output of a background free SHG auto-correlator. The measured field of the FROG spectrogram, $\sqrt{I(\omega,\tau)}$ is shown in Fig. 15(a). Numerical processing then symmetrizes the trace and removes spurious background and noise. The FROG algorithm converges to the spectrogram shown in Fig. 15(b). The FROG algorithm discretizes the measurement into a 512x512 array. The FROG error between the measured and the converged calculated profile, defined as $E_{FROG} \equiv \sqrt{\frac{1}{N^2}\sum_{i,j=1}^{N}\left[I^{meas}_{FROG}(\omega_i,\tau_j) - I^{calculated}_{FROG}(\omega_i,\tau_j)\right]^2}$, where N=512 is the array dimension, is 5.3x10^{-3}.
The intensity profile corresponding to FROG spectrum of Fig. 15(b) is shown in Fig. 16(a). The

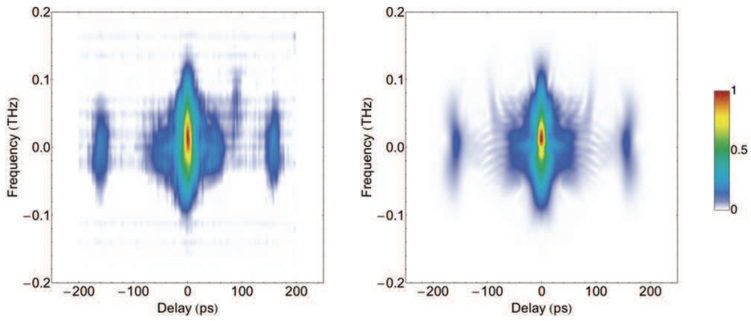

(a) (b)

Fig. 15. Experimental measurement of the 800 mJ pulse duation. (a) Field of the experimentally measured FROG spectrogram. (b) Lowest error field obtained by a FROG algorithm using a 512×512 discretization grid.

pulse is slightly asymmetric and contains a small pre-pulse, caused by a small residual TOD mismatch. We calculate that the FWHM is 8.3 ps, with 84% of the pulse energy contained in the 20 ps wide bin indicated by the dashed box, and the temporal strehl ratio is 0.78. The temporal strehl is the ratio of the peak measured intensity, and the peak transform limited intensity for the measured spectral profile. The temporal waveform on the logarithmic scale (Fig. 16(b)) shows a post pulse at 160 ps, 100 dB lower than the main pulse. This post-pulse causes the satellite wings and the fringing in the FROG measurement. Frequency doubling will further improve the pulse contrast.
FROG also measures the pulse spectrum (Fig. 17). Comparing the FROG measured spectrum with the direct IR spectral measurement performed with an f=1 m spectrometer indicates good agreement.

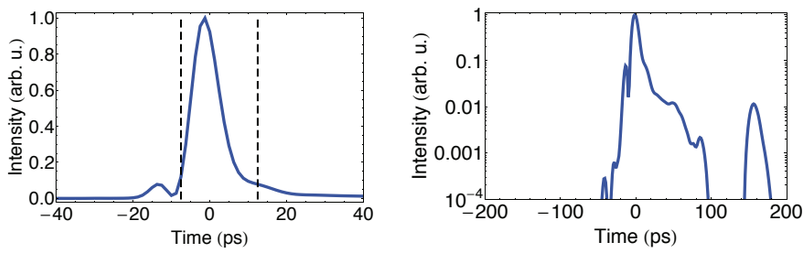

(a) (b)

Fig. 16. Temporal pulse intensity obtained by analyzing a numerically processed FROG spectrogram on the linear scale (a) and log scale (b). FWHM of the pulse duration is 8.3 ps, and 84% of the energy is contained in the 20 ps bin (dashed box).

5. Frequency conversion

High power, high energy laser technology is well developed in the 800 nm to 1.1 μm wavelength range. One can generate other wavelengths through a nonlinear conversion process. Fundamentally, the response of a dielectric medium to an applied electric field can be described by an induced polarization, $\boldsymbol{P} = \epsilon_0 \boldsymbol{\chi}^{(1)} \boldsymbol{E} + \epsilon_0 \boldsymbol{\chi}^{(2)} \boldsymbol{E}\boldsymbol{E} + ...$, where ϵ_0 is the free space permittivity, $\boldsymbol{\chi}^{(n)}$ is the nth order susceptibility, and $\boldsymbol{E}$ is the vector electric field. Because

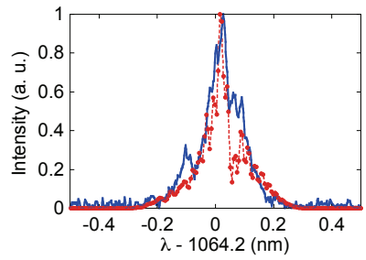

Fig. 17. Pulse spectrum from FROG (red dots) and spectrometer (solid line) measurements.

$\chi^{(1)} \gg \chi^{(2)}$ for an off-resonant medium, higher order terms become important only when the applied electric field is sufficiently high. In a $\chi^{(2)}$ process, $\boldsymbol{EE}$ term produces excitation at twice the fundamental frequency. Let $\boldsymbol{E} = \boldsymbol{A}\cos(\omega t)$, then $\boldsymbol{E}^2 = \frac{A^2}{2}(1 + \cos(2\omega t))$. The magnitude of the nonlinear susceptibility varies with the applied frequency and depends on the electronic level structure of the material. Under well-optimized conditions harmonic efficiencies can exceed 80%. When selecting an appropriate nonlinear crystal, we consider various application dependent factors such as the magnitude of the nonlinear coefficient, acceptance bandwidth, absorption, thermal acceptance, thermal conductivity, walk-off angle, damage threshold, and maximum clear aperture. For pulse durations in the 200 fs to 10 ps range and for the fundamental wavelength $\approx$1 μm, beta barium borate (BBO) is an excellent candidate for 2ω, 3ω, and 4ω generation. The main draw back, is that the largest clear crystal aperture is $\approx$20 mm which limits its use to low pulse energies ($< 10 - 100$ mJ). For higher pulse energies, deuterated and non-deuterated potassium dihydrogen phosphate (DKDP and KDP), lithium triborate (LBO) and yttrium calcium oxyborate (YCOB) can be grown to much larger apertures. YCOB is particularly attractive for its high average power handling, high damage threshold, and large effective nonlinearity (Liao et al., 2006). For frequency doubling, typical required laser intensities are in the 100 MW/cm^2 to 10 GW/cm^2 range.

The crystal must be cut along an appropriate plane to allow phase matching and to maximize the effective nonlinear coefficient, d_{eff}, which is related to $\chi^{(2)}$ and the crystal orientation. The interacting waves at ω and 2ω acquire different phases, $\phi(\omega) = k_\omega z = n_\omega \omega z/c$ and $\phi(2\omega) = k_{2\omega} z = 2n_{2\omega}\omega z/c$ as they propagate along the crystal in z direction. An interaction is phase matched when $k_{2\omega} = 2k_\omega$. A uniaxial crystal contains two polarization eigenvectors, one parallel to the optic axis (the axis of rotation symmetry) and one perpendicular to it. An electric field inside the crystal contains a component perpendicular to the optic axis (ordinary polarization) and a component in the plane defined by the optic axis and the direction of propagation (extraordinary polarization), as illustrated in Fig. (18). The refractive index of the extraordinary polarization, n^e, varies with θ, the angle between the direction of propagation and the optic axis; the ordinary refractive index, n^o has no angular dependence. In the example shown in Fig. (18), the crystal is rotated along the y-axis until $n^e_{2\omega}(\theta) = n^o_\omega$. The illustrated phase matching condition, where both incident photons have the same polarization is known as type I phase matching. In Type II phase matching, the incident field has both an ordinary and an extraordinary polarization component.

Coupled Eqs. (14-15), given in SI units, describe Type I, 2ω generation process relevant for 200 fs - 10 ps duration pulses. Here, we make a plane wave approximation, justified when we are not focusing into the crystal, and when the crystal is sufficiently thin to ignore beam walk-off effects. We also ignore pulse dispersion in the crystal, justified for our pulse bandwidth and crystal thickness. We can account for two-photon absorption, which becomes

important for 4ω generation in BBO, by adding $\beta|A_{2\omega}|^2 A_{2\omega}$ term to the left hand side of Eq. (15).

$$\frac{\partial A_\omega}{\partial z} + \frac{1}{v_{g,\omega}}\frac{\partial A_\omega}{\partial t} + \frac{\alpha_\omega}{2}A_\omega = i\frac{2\omega}{n(\omega)c}d_{eff}A^*_\omega A_{2\omega}\exp(-i\Delta kz) \tag{14}$$

$$\frac{\partial A_{2\omega}}{\partial z} + \frac{1}{v_{g,2\omega}}\frac{\partial A_{2\omega}}{\partial t} + \frac{\alpha_{2\omega}}{2}A_{2\omega} = i\frac{2\omega}{n(2\omega)c}d_{eff}A^2_\omega \exp(i\Delta kz) \tag{15}$$

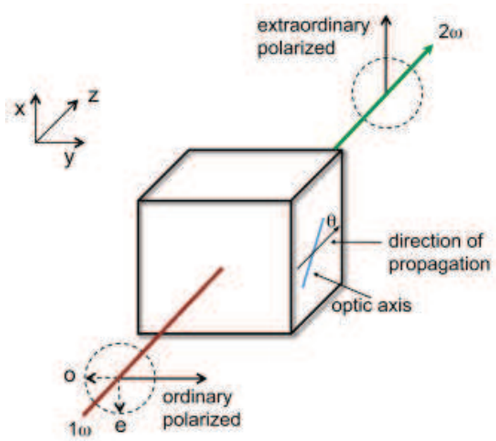

Fig. 18. Frequency doubling with OOE type phasematching in a uniaxial nonlinear crystal. θ is the phasematching angle between the optic axis and the propagation direction.

We obtain an analytical solution assuming qausi-CW pulse duration, which eliminates the time dependent terms, and a low conversion efficiency, or a constant A_ω. The efficiency of 2ω harmonic generation, $\eta_{2\omega} = I_{2\omega}/I_\omega$, reduces to Eq. (16):

$$\eta_{2\omega} = \frac{8\pi^2 d^2_{eff} L^2 I_\omega}{\epsilon_0 n^2_\omega n_{2\omega} c\lambda^2_\omega}\frac{\sin^2(\Delta kL/2)}{(\Delta kL/2)^2} \tag{16}$$

In our laser systems, we implement frequency conversion on both, the photogun and the interaction laser systems (Gibson et al., 2010). On T-REX, we generate the 4^{th} harmonic of the fundamental frequency by cascading two BBO crystals. The first, 1 mm thick crystal cut for Type I phase matching, frequency doubles the incident pulse from 1053 nm to 527 nm. The second 0.45 mm thick BBO crystal cut for Type I phase matching,frequency doubles 527 nm pusle to 263 nm. The overall conversion efficiency from IR to UV is 10%, yielding 100 μJ at 263 nm. Here, frequency conversion is primarily limited by two-photon absorption in the UV and the group velocity mismatch (GVM) between the 2ω and the 4ω pulses. GVM results in temporal walk-off of the pulse envelopes and, in the frequency domain, is equivalent to the acceptance bandwidth.

On the interaction laser, we frequency double the high energy pulses to increase the final γ-ray energy. On T-REX we use a large aperture (30x30 mm) 6 mm thick DKDP crystal to frequency double 800 mJ pulse from 1064 nm to 532 nm with up to 40% conversion efficiency. Here, the pulse bandwidth is relatively narrow ($\approx$0.2 nm) and group velocity walk-off is insignificant. The conversion efficiency is primarily limited by beam quality and temporal pulse shape. Generated 532 nm pulse energy is plotted vs the compressed input pulse energy in Fig. 19.

At maximum IR energy, the conversion efficiency unexpectedly decreases. This may indicate onset of crystal damage, degradation in pulse quality, or an increase in phase mismatch.

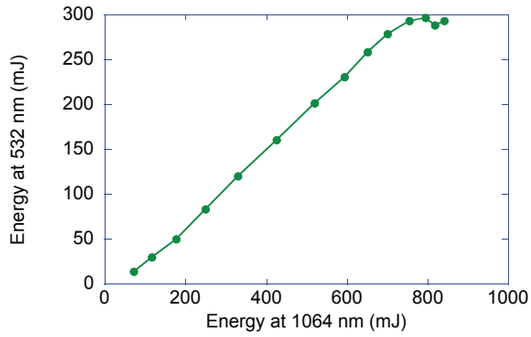

Fig. 19. Frequency doubling of the 10 ps T-REX ILS laser with a peak efficiency of 40%.

6. Pulse shaping

A uniform elliptical laser shape in space and time minimizes the contribution of space-charge force on the electron beam emittance (Kapchinskij & Vladimirskij, 1959; Li & Lewellen, 2008). Due to technical difficulties of generating this shape, simulations suggest that a uniform cylindrical pulse in space and time is an alternative (Cornacchia & *et. al.*, 1998). We generate the cylindrical shape by time-stacking the UV laser pulse in a Hyper-Michelson interferometer (Siders et al., 1998) and clipping the UV beam with a hard edge aperture. It is also possible to mode-convert the UV beam from a Gaussian to a flat-top with a commercial refractive beam shaper based on aspheric lenses.

The pulse shaper is a Michelson-based ultrafast multiplexing device having nearly 100% throughput and designed for high energy shaped pulse generation. The pulse train generates a train of replicas of the input pulse delayed with respect to each other with femtosecond precision. The pulse stacker used in T-REX (Gibson et al., 2010) consists of 4 stages, stacking 16 pulses. The laser pulse passes through a series of beam splitters, each time being recombined following an adjustable delay path. The built pulse stacker is shown in Fig. 20. At the output of the pulse stacker, two orthogonally polarized pulse trains are recombined and interleaved in time at a polarizing beamsplitter. The individual pulses must be sufficiently delayed to avoid high frequency intensity modulation that results from interferences of same-polarized pulses.

An example of a stacked flat-top pulse from the pulse stacker is shown in Fig. 21. The figure shows a cross-correlation of the stacked UV pulse obtained on T-REX. The 15 ps stacked UV (4ω) pulse is cross-correlated with the $\approx$0.75 ps IR (1ω) pulse (blue line). The predicted cross-correlation on the basis of the pulse energies of each of the 16 stacked pulses is shown by the dashed line. Cross-correlations between the IR and the 16 individual UV pulses are shown below the main pulse.

7. High energy laser pulse recirculation

In this section we describe a novel technique for recirculating high power, high energy, picosecond laser pulses, akin to the interaction laser pulses on T-REX. The motivation for laser recirculation for compton-scattering sources is two-fold. First, a major fundamental limitation of these sources is the extremely small Thomson scattering cross-section, $\sigma_T = \frac{8\pi}{3} r_e^2 = 6.65 \times 10^{-25}\text{cm}^2$, where r_e classical electron radius, which leads to low conversion

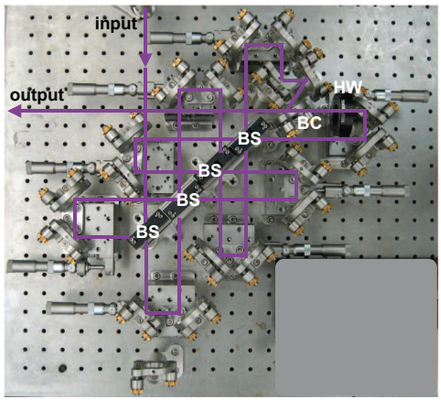

Fig. 20. Photograph of the pulse stacker on T-REX photogun laser.

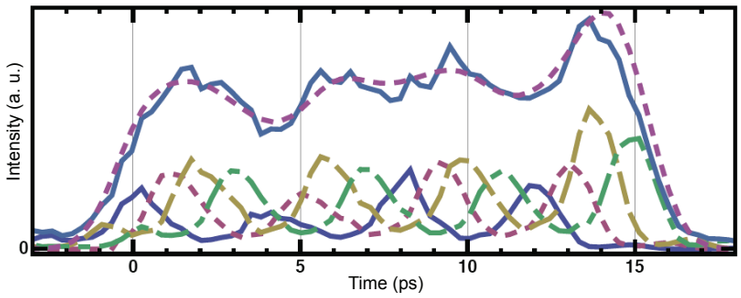

Fig. 21. Cross-correlation measurement of the temporally shaped UV pulse from T-REX photogun laser indicates a 15 ps FWHM pulse duration.

efficiency from laser photons to γ rays. Only 1 in 10^{10} of laser photons is doppler upshifted to γ-ray energy. The overall efciency of the compton-scattering source could be increased by reusing the laser photons after each interaction with the electron bunch. Second, the joule-class, short pulse lasers operate at a few Hz to 100 Hz type of repetition rates. Linacs can operate at kHz and higher repetition rates. Increasing the repetition rate of the interaction laser would increase the average brightness of the γ-ray source.

The pulse recirculation scheme that we have developed is general and could be applied to various other phenomena that involve high intensity lasers interacting with an optically thin medium such as cavity ring down spectroscopy, high-harmonic generation in short gas jets, or laser based plasma diagnostics. The pulse recirculation scheme is based on injection and trapping a single laser pulse inside a passive optical cavity. A thin nonlinear crystal acts as an optical switch, trapping the frequency converted light. This technique, termed recirculation injection by nonlinear gating (RING) is compatible with joule class, 100s of Watts of average power, picosecond laser pulses. In the simplest implementation of this technique, the incident laser pulse at the fundamental frequency enters the resonator and is efficiently frequency doubled. The resonator mirrors are dichroic, coated to transmit the 1ω light and reflect at 2ω (see Fig. 22). The upconverted 2ω pulse becomes trapped inside the cavity. After many roundtrips, the laser pulse decays primarily due to Fresnel losses at the crystal faces and cavity mirrors. The crystal thickness is optimized for high conversion efficiency.

Current pulse recirculation schemes are based on either resonant cavity coupling (Gohle et al., 2005; Jones et al., 2005) or active (electro-optic or acousto-optic) pulse switching (Yu & Stuart,

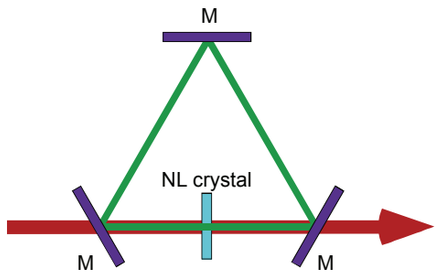

Fig. 22. Conceptual design of the RING picosecond pulse recirculation cavity.

1997; Mohamed et al., 2002) into and out of the resonator. Active pulse switching schemes are suitable for low intensity, nanosecond duration pulses (Meng et al., 2007). Resonant cavity coupling requires interferometric cavity alignment and MHz and higher repetition rates. To date, researchers have attained up to 100x enhancement for 1 W average power, ≈50 fs duration incident pulses with per pulse energy <1 μJ. Compared to active pulse switching schemes, the main advantage of RING is an order of magnitude reduction of the accumulated nonlinear phase with each roundtrip. Here, the crystal thickness is a few mm, compared to a few cm thick crystal inside a pockels cell. Compared to resonant cavity coupling, RING increases the intracavity repetition rate, while maintaining nearly the same peak pulse power. A resonant cavity increases the peak pulse power while decreasing the intracavity repetition rate.

We describe a low energy, millijoule-scale and a high energy, joule-scale pulse recirculation experiments (Shverdin, Jovanovic, V. A. Semenov, Brown, Gibson, Shuttlesworth, Hartemann, Siders & Barty, 2010). We chose a Fabry-Perot configuration for our RING cavity to maximize the cavity finesse (Fig. 23). In this arrangement, the concave spherical mirrors are spaced $\approx 2f$ apart, where $f = 375$ mm is the focal length of each of the cavity mirrors. The mirrors' multi-layer dielectric coating on the surface internal to the cavity is 99.8% reflective at 527 nm and 98% transmissive at 1053 nm. The mirrors' flat surface external to the cavity is anti-reflection coated at both wavelengths. Any plane inside the cavity is relay imaged back onto itself, which minimizes diffraction losses and supports an arbitrary incident spatial profile. The difference in the RING cavity designs for the two experiments involves the aperture size of the optical components and the choice of the doubling crystal.

The CAD experimental design is shown in Fig. 24. The cavity is contained inside two interconnected vacuum chambers. One of the vacuum chambers contains the nonlinear crystal and one of the spherical mirrors. The second chamber contains the other spherical mirror. Concave spherical mirrors act as negative lenses in transmission. A positive lens prior to the cavity adjusts the beam curvature to produce a collimated wavefront for the input 1ω (IR) beam inside the cavity. The 2ω beam is collimated when traveling from right to left, and focuses in the middle when traveling in the opposite direction. The cavity contains an internal focus to simulate an electron beam interaction region. Vacuum compatible actuators control the tip/tilt of the mirrors, the phase matching angle of the crystal, and the total cavity length. The chambers are pumped down to 10^{-3} Torr range to minimize nonlinear phase accumulation and prevent air breakdown at the focus.

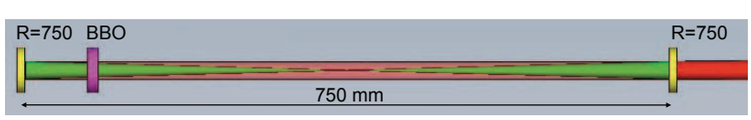

Fig. 23. Ray trace of the designed confocal resonator-type RING cavity.

In the low energy experiment, we inject a 10 Hz, 1.7 mJ, 10 nm bandwidth pulse centered at 1053 nm and chirped to 2.25 ps through the right 1" diameter cavity mirror, which is a negative lens in transmission. Upstream beam sizing optics produce a collimated w_0=4 mm gaussian inside the cavity. The nonlinear crystal is a 10x10x1 mm Type I SHG BBO crystal. The crystal has a single layer MgF_2 antireflection (AR) coating at both wavelengths (0.3% loss per surface). The choice of BBO is motivated by its excellent thermomechanical properties, broad spectral and thermal acceptance, and a relatively low nonlinear index to effective nonlinear coefficient ratio, n_2/d_{eff}. We measure 270 μJ at 527 nm after the crystal, corresponding to peak intensity ≈ 0.8 GW/cm^2. The majority of the residual IR is coupled out of the cavity through the end mirror.

The precise cavity length, L_{cav}, is slightly longer than $2f$ to account for refraction through the crystal. $L_{cav} = 2f + \Delta L$, where ΔL=L_c(1-1/n_c). Here, L_c is the crystal's thickness and n_c is its refractive index at 2ω. ΔL=2 mm for the 1 mm thick BBO.

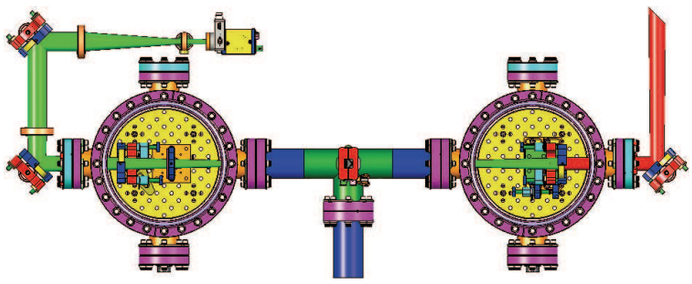

Fig. 24. CAD of the RING cavity design: two interconnected vacuum chambers contain the nonlinear crystal and dichroic mirrors.

We measure cavity enhancement at 2ω, by recording the leakage 527 nm light that passes through the end mirror, on a 1.2 GHz Si photodiode and 15 GHz digital signal oscilloscope and analyzing the resulting cavity ring-down signal. We define enhancement as $enh \equiv \sum_{n=0}^{N} I_n / I_0$, where I_n is pulse power after n roundtrips, and N is the total number of roundtrips. Dichroic mirrors and green bandpass filters scrape off any residual IR from the detected beam. The measured ring-down signal (Fig. 25) shows approximately 170 pulses spaced by the 5 ns, cavity roundtrip time. Impedance mismatch between the photodiode and the oscilloscope introduces some ringing in the recorded waveform.

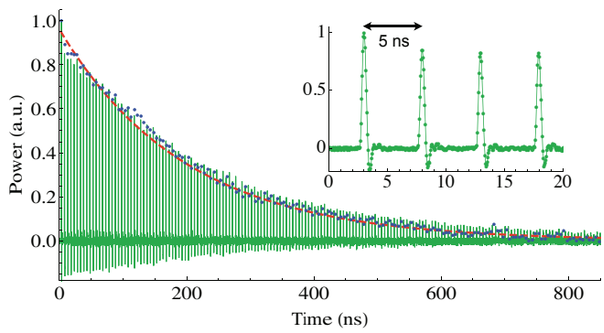

Fig. 25. Low energy cavity ring-down signal indicates 40x signal enhancement. The red dashed line is an exponential fit to the pulse power at each roundtrip (blue circles). The total cavity length sets the 5 ns pulse spacing (inset figure).

The circles in Fig. 25 correspond to the normalized power in each pulse, determined by integrating the voltage signal. The expected power in each successive pulse is $(1-\alpha)$ times the power of the previous pulse, or I_n=$I_0(1-\alpha)^n$, where I_0 is the initial signal power and α is the loss per roundtrip. The total cavity enhancement is then [1-(1-α)^n]/α. The dashed line in the figure is a fit to pulse power with α = 0.025, corresponding to *enh*=40. Contributions above the 1.8% Fresnel losses, could be attributed to hard edge diffraction and scattering in the nonlinear crystal. In the measured trace, the ratio of the powers in the first to the second pulses is larger than for subsequent pulses; an effect caused by additional diffraction losses during the first pass. The waveform also exhibits "picket fence" effect, where the power of many pulses is higher than of the adjacent pulses. This is likely caused by a slight cavity misalignment. We explicitly calculate cavity enhancement by summing over all of the observed pulses, obtaining *enh*=36. We estimate the total accumulated nonlinear phase, ϕ_{NL}=$\frac{2\pi n_2 L_c I_{peak}}{\lambda}\frac{1-(1-\alpha)^N}{\alpha}$=0.7 rad, where, n_2 is the nonlinear refractive index (8.8x10^{-16} cm^2/W).

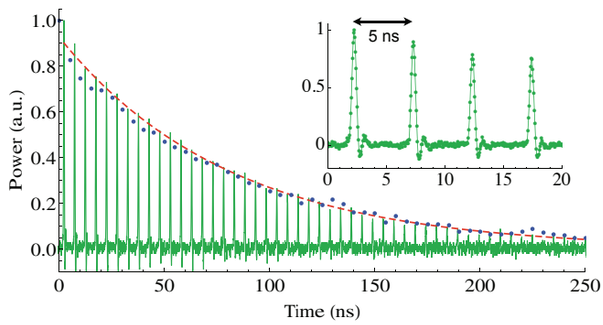

Fig. 26. High energy (177 mJ) cavity ring-down signal indicates 17x signal enhancement.

In the high energy experiment, both the spatial and the temporal profiles exhibited significant aberrations. We injected 10 Hz, 677 mJ, 0.25 nm bandwidth pulses at 1064 nm with a FWHM pulse duration of 20 ps. Autocorrelation measurements of the IR pulse indicate that 70% of the 677 mJ is contained in a wide 400 ps pulse pedestal. Compared to the low energy experiment, the main changes to the RING cavity involve replacing 1" diameter cavity mirrors with 2" diameter mirrors and replacing the small aperture BBO crystal with 30x30x6 mm deuterated potassium dihydrogen phosphate (DKDP) cut for Type II phase matching. After frequency doubling, we generate 177 mJ at 532 nm in an slightly elliptical 12x15 mm FWHM beam. Computer simulations indicate that the pulse at 532 nm is 16 ps FWHM and 50% of total energy is contained in the wide pedestal. We estimate the resulting peak pulse intensity at 4 GW/cm^2.

The high energy ring-down signal is shown in Fig. 26. We observe pulses over ≈50 roundtrips. Here, the loss coefficient, α=0.06, resulting in cavity enhancement, *enh*=17, the same value as obtained by explicitly summing the powers in each pulse. The estimated total nonlinear phase is 2.8 rad. We attribute the significant degradation in cavity enhancement to the poor spatial beam quality of the high energy 1ω laser. The near field spatial profile suffers from high frequency intensity modulation causing high hard edge diffraction losses at the crystal. When we replaced the DKDP crystal with a smaller aperture 20x20x1.2 mm BBO crystal, higher diffraction losses reduced cavity enhancement to 11.

The peak power scaling of the RING cavity is primarily limited by the nonlinear phase accumulation in the crystal. For a gaussian pulse, the bandwidth doubles for ϕ_{NL}≈2.4.

In monoenergetic gamma-ray generation, this increases the bandwidth of the generated photons (Albert et al., 2010). Other deleterious effects include whole beam self-focusing and modulation instability growth. Increasing beam size and correspondingly the aperture of the cavity optics mitigates nonlinear phase accumulation. DKDP crystals are available in sizes up to 40x40 cm, potentially enabling recirculation of 100 J, 10 ps pulses.

RING cavity design is scalable to very high peak and average power recirculation. Linear absorption in the crystal is the primary limitation to the maximum sustainable average power inside the cavity. LBO, YCOB, and BBO crystals are particularly attractive candidates for high average power operation. For a simple edge cooling scheme, finite element simulation of the thermal profile inside the crystal indicate that LBO and YCOB support up to 1.2 kW of total recirculating power. The peak recirculating power limit could be significantly increased with surface cooling schemes.

Deploying RING on a Compton scattering light source could lead to more than an order of magnitude increase in average source brightness of the generated γ-ray flux. The RING cavity would be integrated into the γ-ray source after a relatively simple modification of the interaction point architecture.

8. Conclusion

We provided a brief overview of Compton-scattering based compact monoenergetic γ-ray sources, emphasizing the recently commissioned 2^{nd} generation T-REX, and the currently under construction, 3^{rd} generation Velociraptor machine at LLNL. We detailed the underlying laser technology and described several technological breakthroughs which enable development of γ-ray sources with the highest peak brightness in a compact footprint.

We expect continued improvement in future Compton-based light sources. In the laser realm, some of the fruitful future research will include: (1) boosting the laser repetition rates to develop joule-class, kW and MW average power systems, to increase the average γ-ray source brightness; (2) developing tunable and multi-resonant joule-class, picosecond optical parametric amplifiers, to either simultaneously generate multiple γ-ray energies or rapidly tune the output energy; (3) preparing proper laser pulse and beam formats to further reduce the γ-ray bandwidth; (4) demonstrating appropriate beam pointing and scanning technology to enable γ-ray beam rastering.

This work was performed under the auspices of the U.S. Department of Energy by University of California, Lawrence Livermore National Laboratory under Contract W-7405-ENG- 48. We also acknowledge support of DOE/NA-22.

9. References

Albert, F., Anderson, S. G., Anderson, G. A., Betts, S. M., Gibson, D. J., Hagmann, C. A., Hall, J., Johnson, M. S., Messerly, M. J., Semenov, V. A., Shverdin, M. Y., Tremaine, A. M., Hartemann, F. V., Siders, C. W., McNabb, D. P. & Barty, C. P. J. (2010). Isotope-specific detection of low-density materials with laser-based monoenergetic gamma-rays, *Opt. Lett.* 35(3): 354–356.

Arutyunyan, F. R. & Tumanyan, V. A. (1964). Quasi-monochromatic and polarized high-energy gamma rays, *Soviet Physics Uspekhi* 7(3): 339.

Bech, M., Bunk, O., David, C., Ruth, R., Rifkin, J., Loewen, R., Feidenhans, R. & Pfeiffer, F. (2009). Hard x-ray phase-contrast imaging with the compact light source based on inverse compton x-rays, *J. Synchrotron Radiat.* 16: 43–47.

Bertozzi, W. & Ledoux, R. J. (2005). Nuclear resonance fluorescence imaging in non-intrusive cargo inspection, *Nucl. Instrum. Meth. B* 241: 820–825.

Carroll, F. E., Mendenhall, M. H., Traeger, R. H., Brau, C. & Waters, J. W. (2003). Pulsed tunable monochromatic x-ray beams from a compact source: New opportunities, *Am. J. Roentgenol.* 181: 1197–1202.

Cheriaux, G., Rousseau, P., Salin, F., Chambaret, J. P., Walker, B. & Dimauro, L. F. (1996). Aberration-free stretcher design for ultrashort-pulse amplification, *Opt. Lett.* 21: 414–416.

Compton, A. H. (1923). A quantum theory of the scattering of x-rays by light elements, *Phys. Rev.* 21(5): 483–502.

Cornacchia, M. & *et. al.* (1998). Linac coherent light source (lcls) design study report, *Technical report*, SLAC-R-521, Stanford Linear Accelerator Center, Stanford, CA.

D'Angelo, A., Bartalini, O., Bellini, V., Sandri, P. L., Moricciani, D., Nicoletti, L. & Zucchiatti, A. (2000). Generation of compton backscattering [gamma]-ray beams, *Nucl. Instrum. Meth. A* 455(1): 1–6.

Duarte, F. J. (1987). Generalized multiple-prims dispersion theory for pulse compression in ultrafast dye lasers, *Opt. Quant. Electron.* 19: 223–229.

Esarey, E., Ride, S. K. & Sprangle, P. (1993). Nonlinear thomson scattering of intense laser pulses from beams and plasmas, *Phys. Rev. E* 48(4): 3003–3021.

Feenberg, E. & Primakoff, H. (1948). Interaction of cosmic-ray primaries with sunloght and starlight, *Phys. Rev.* 73(5): 449–469.

Fittinghoff, D. N., Molander, W. A. & Barty, C. P. J. (2004). Hyperdispersion grating arrangements for compact pulse compressors and expanders, *Frontiers in Optics*, Optical Society of America, Rochester, NY, p. FThL5.

Forster, R. A., Cox, L. J., Barrett, R. F., Booth, T. E., Briesmeister, J. F., Brown, F. B., Bull, J. S., Geisler, G. C., Goorley, J. T., Mosteller, R. D., Post, S. E., Prael, R. E., Selcow, E. C. & Sood, A. (2004). Mcnp(tm) version 5, *Nucl. Instrum. Meth. B* 213: 82–86.

Frantz, L. M. & Nodvik, J. S. (1963). Theory of pulse propagation in a laser amplifier, *J. Appl. Phys.* 34: 2346–2349.

Gibson, D. J., Albert, F., Anderson, S. G., Betts, S. M., Messerly, M. J., Phan, H. H., Semenov, V. A., Shverdin, M. Y., Tremaine, A. M., Hartemann, F. V., Siders, C. W., McNabb, D. P. & Barty, C. P. J. (2010). Design and operation of a tuna ble mev-level compton-scattering-based γ-ray source, *PRST-AB* vol. 13, page 070703 (2010).

G.Matt, Feroci, M., Rapisarda, M. & Costa, E. (1996). Treatment of compton scattering of linearly polarized photons in monte carlo codes, *Radiat. Phys. Chem.* 48(4): 403–411.

Gohle, C., Udem, T., Herrmann, M., Rauschenberger, J., Holzwarth, R., Schuessler, H., Krausz, F. & Hänsch, T. (2005). A frequency comb in the extreme ultraviolet, *Nature* 436: 234–237.

Graves, W. S., Brown, W., Kartner, F. X. & Moncton, D. E. (2009). Mit inverse compton source concept, *Nucl. Instrum. Meth. A* 608(1, Supplement 1): S103–S105.

Hartemann, F. (2002). *High Field Electrodynamics*, CRC Press, Boca Raton, FL.

Hartemann, F. V. & Kerman, A. K. (1996). Classical theory of nonlinear compton scattering, *Phys. Rev. Lett.* 76(4): 624–627.

Ilday, F., Buckley, J., Lim, H., Wise, F. & Clark, W. (2003). Generation of 50-fs, 5-nj pulses at 1.03 μm from wave-breaking free fiber laser, *Opt. Lett.* 28: 1365–1367.

Jeong, Y., Sahu, J. K. & Nilsson, J. (2004). Ytterbium-doped large-core fiber laser with 1.36 kw continuous-wave output power, *Opt. Express* 12: 6088–6092.

Jones, R. J., Moll, K. D., Thorpe, M. J. & Ye, J. (2005). Phase-coherent frequency combs in the vacuum ultraviolet via high-harmonic generation inside a femtosecond enhancement cavity, *Phys. Rev. Lett.* 94: 193201.

Kane, D. J., Taylor, A. J., Trebino, R. & DeLong, K. W. (1994). Single-shot measurement of the intensity and phase of a femtosecond uv laser pulse with frequency-resolved optical gating, *Opt. Lett.* 19: 1061–1063.

Kane, D. J. & Trebino, R. (1993). Single-shot measurement of the intensity and phase of an arbitrary ultrashort pulse by using frequency-resolved optical gating, *Opt. Lett.* 18: 823–825.

Kapchinskij, I. M. & Vladimirskij, V. V. (1959). Limitations of proton beam current in a strong focusing linear accelerator associated with beam space charge, *in* L. Kowarski (ed.), *Conference on High Energy Accelerators and Instrumentation*, CERN, p. 274.

Kawase, K., Kando, M., Hayakawa, T., Daito, I., Kondo, S., Homma, T., Kameshima, T., Kotaki, H., Chen, L.-M., Fukuda, Y., Faenov, A., Shizuma, T., Fujiwara, M., Bulanov, S. V., Kimura, T. & Tajima, T. (2008). Sub-mev tunably polarized x-ray production with laser thomson backscattering, *Rev. Sci. Instrum.* 79: 053302.

Kostenbauder, A. G. (1990). Ray-pulse matrices: A rational treatment for dispersive optical systems, *IEEE J. Quantum Elect.* 26: 1148–1157.

Leemans, W., Schoenlein, R., Volfbeyn, P., Chin, A., Glover, T., Balling, P., Zolotorev, M., Kim, K.-J., Chattopadhyay, S. & Shank, C. (1997). Interaction of relativistic electrons with ultrashort laser pulses: generation of femtosecond x-rays and microprobing of electron beams, *IEEE J. Quantum Elect.* 33(11): 1925–1934.

Li, Y. & Lewellen, J. (2008). Generating a quasiellipsoidal electron beam by 3d laser-pulse shaping, *Phys. Rev. Lett.* 100: 074801.

Liao, Z. M., Jovanovic, I. & Ebbers, C. A. (2006). Energy and average power scalable optical parametric chirped-pulse amplification in yttrium calcium oxyborate, *Opt. Lett.* 31(9): 1277–1279.

Lin, Q., Wang, S., Alda, J. & Bernabeu, E. (1993). Transformation of pulsed nonideal beams in a four-dimension domain, *Opt. Lett.* 18: 669–671.

Litvinenko, V. N., Burnham, B., Emamian, M., Hower, N., Madey, J. M. J., Morcombe, P., O'Shea, P. G., Park, S. H., Sachtschale, R., Straub, K. D., Swift, G., Wang, P., Wu, Y., Canon, R. S., Howell, C. R., Roberson, N. R., Schreiber, E. C., Spraker, M., Tornow, W., Weller, H. R., Pinayev, I. V., Gavrilov, N. G., Fedotov, M. G., Kulipanov, G. N., Kurkin, G. Y., Mikhailov, S. F. & Popik, V. M. (1997). Gamma-ray production in a storage ring free-electron laser, *Phys. Rev. Lett.* 78: 4569–4572.

Martinez, O. E. (1987). 3000 times grating compressor with positive group velocity dispersion: Application to fiber compensation in 1.3-1.6 μm region, *IEEE J. Quantum Elect.* 23: 59–64.

Meng, D., Sakamoto, F., Yamamoto, T., Dobashi, K., Uesaka, M., Nose, H., Ishida, D., Kaneko, N. & Sakai, Y. (2007). High power laser pulse circulation experiment for compact quasi-monochromatic tunable x-ray source, *Nucl. Instrum. Meth. B* 261: 52.

Milburn, R. H. (1963). Electron scattering by an intense polarized photon field, *Phys. Rev. Lett.* 10(3): 75–77.

Mohamed, T., Andler, G. & Schuch, R. (2002). Development of an electro-optical device for storage of high power laser pulses, *Opt. Commun.* 214: 291–295.

Perry, M. D., Boyd, R. D., Britten, J. A., Decker, D., Shore, B. W., Shannon, C. & Shults, E. (1995). High-eff iciency multilayer dielectric diffraction gratings, *Opt. Lett.* 20: 940–942.

Pietralla, N., Berant, Z., Litvinenko, V. N., Hartman, S., Mikhailov, F. F., Pinayev, I. V., Swift, G., Ahmed, M. W., Kelley, J. H., Nelson, S. O., Prior, R., Sabourov, K., Tonchev, A. P. & Weller, H. R. (2002). Parity measurements of nuclear levels using a free-electron-laser generated γ-ray beam, *Phys. Rev. Lett.* 88(1): 012502.

Planchon, T. A., Burgy, F., Rousseau, J.-P. & Chambaret, J.-P. (2005). 3d modeling of amplification processes in cpa laser amplifiers, *Appl. Phys. B* 80: 661–667.

Pruet, J., McNabb, D. P., Hagmann, C. A., Hartemann, F. V. & Barty, C. P. J. (2006). Detecting clandestine material with nuclear resonance fluorescence, *J. Appl. Phys.* 99: 123102.

Shverdin, M. Y., Albert, F., Anderson, S. G., Betts, S. M., Gibson, D. J., Messerly, M. J., Hartemann, F., Siders, C. W. & Barty, C. P. J. (2010). Chirped pulse amplification with narrowband pulses, *Opt. Lett.* 35: 2478–2480.

Shverdin, M. Y., Jovanovic, I., V. A. Semenov, S. M. B., Brown, C., Gibson, D. J., Shuttlesworth, R. M., Hartemann, F. V., Siders, C. W. & Barty, C. P. J. (2010). High-power picosecond laser pulse recirculation, *Opt. Lett.* 35: 2224–2226.

Siders, C. W., Siders, J. L. W., Taylor, A. J., Park, S.-G. & Weiner, A. M. (1998). Efficient high-energy pulse-train generation using a 2 n-pulse michelson interferometer, *App. Opt.* 37: 5302–5305.

Strickland, D. & Mourou, G. (1985). Isotope-specific detection of low density materials with laser-based mono-energetic gamma-rays, *Opt. Commun.* 56(219-221).

Sumetsky, M., Eggleton, B. & de Sterke, C. (2002). Theory of group delay ripple generated by chirped fiber gratings, *Opt. Express* 10: 332–340.

Titov, A. I., Fujiwara, M. & Kawase, K. (2006). Parity non-conservation in nuclear excitation by circularly polarized photon beam, *J. Phys. G: Nucl. Part. Phys.* 32: 1097–1103.

Treacy, E. B. (1969). Optical pulse compression with diffraction gratings, *IEEE J. Quantum Elect.* 5(454-458).

Trebino, R. (2000). *Frequency-Resolved Optical Gating: The Measurement of Ultrashort Laser Pulses*, Kluwer Academic Publishers, Boston, MA.

Yakimenko, V. & Pogorelsky, I. V. (2006). Polarized γ source based on compton backscattering in a laser cavity, *Phys. Rev. Spec. Top.-AC* 9: 091001.

Yu, D. & Stuart, B. (1997). A laser pulse trapper for compton backscattering applications, *Particle Accelerator Conference*, PAC'97, Vacouver, DC, Canada.

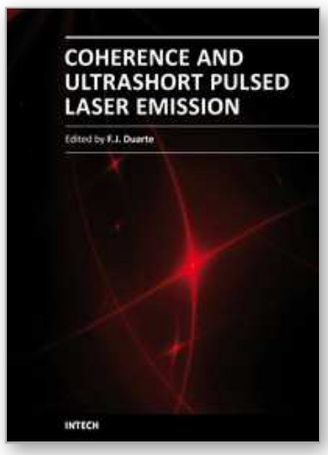

Coherence and Ultrashort Pulse Laser Emission
Edited by Dr. F. J. Duarte

ISBN 978-953-307-242-5
Hard cover, 688 pages
Publisher InTech
Published online 30, November, 2010
Published in print edition November, 2010

In this volume, recent contributions on coherence provide a useful perspective on the diversity of various coherent sources of emission and coherent related phenomena of current interest. These papers provide a preamble for a larger collection of contributions on ultrashort pulse laser generation and ultrashort pulse laser phenomena. Papers on ultrashort pulse phenomena include works on few cycle pulses, high-power generation, propagation in various media, to various applications of current interest. Undoubtedly, Coherence and Ultrashort Pulse Emission offers a rich and practical perspective on this rapidly evolving field.

How to reference
In order to correctly reference this scholarly work, feel free to copy and paste the following:

Miro Shverdin, Fred Hartemann, Felicie Albert, Mike Messerly, David Gibson, Craig Siders and Chris Barty (2010). Laser Technology for Compact, Narrow-bandwidth Gamma-ray Sources, Coherence and Ultrashort Pulse Laser Emission, Dr. F. J. Duarte (Ed.), ISBN: 978-953-307-242-5, InTech, Available from: http://www.intechopen.com/books/coherence-and-ultrashort-pulse-laser-emission/laser-technology-for-compact-narrow-bandwidth-gamma-ray-sources

INTECH
open science | open minds

InTech Europe
University Campus STeP Ri
Slavka Krautzeka 83/A
51000 Rijeka, Croatia
Phone: +385 (51) 770 447
Fax: +385 (51) 686 166
www.intechopen.com

InTech China
Unit 405, Office Block, Hotel Equatorial Shanghai
No.65, Yan An Road (West), Shanghai, 200040, China
中国上海市延安西路65号上海国际贵都大饭店办公楼405单元
Phone: +86-21-62489820
Fax: +86-21-62489821

IntechOpen